Time dependence of advection-diffusion coupling for nanoparticle ensembles

Alexandre Vilquin,[1] Vincent Bertin,[1, 2] Pierre Soulard,[1] Gabriel Guyard,[1, 3]
Elie Raphaël,[1] Frédéric Restagno,[3] Thomas Salez,[2, 4] and Joshua D. McGraw[1]

[1]*Gulliver CNRS UMR 7083, PSL Research University,*
ESPCI Paris, 10 rue Vauquelin, 75005 Paris, France
[2]*Univ. Bordeaux, CNRS, LOMA, UMR 5798, F-33405, Talence, France*
[3]*Université Paris-Saclay, CNRS, Laboratoire de physique des solides, Orsay, France*
[4]*Global Station for Soft Matter, Global Institution for Collaborative*
Research and Education, Hokkaido University, Sapporo, Hokkaido, Japan
(Dated: July 10, 2020)

Particle transport in fluids at micro- and nano-scales is important in many domains. As compared to the quiescent case, the time evolution of particle dispersion is enhanced by coupling: *i*) advection along the flow; and *ii*) diffusion along the associated velocity gradients. While there is a well-known, long-time limit for this advection-diffusion enhancement, understanding the short-time limit and corresponding crossover between these two asymptotic limits is less mature. We use evanescent-wave video microscopy for its spatio-temporal resolution. Specifically, we observe a near-surface zone of where the velocity gradients, and thus dispersion, are the largest within a simple microfluidic channel. Supported by a theoretical model and simulations based on overdamped Langevin dynamics, our experiments reveal the crossover of this so-called Taylor dispersion from short to long time scales. Studying a range of particle size, viscosity and applied pressure, we show that the initial spatial distribution of particles can strongly modify observed master curves for short-time dispersion and its crossover into the long-time regime.

PACS numbers:

Hydrodynamic flows typically exhibit a spatially varying velocity, often as a result of a nearby solid, immobile boundary. When microscopic particles are transported by such a near-surface flow, the coupling between diffusion along the flow gradients and streamwise advection leads to an enhanced dispersion as compared to the no-flow case. This enhancement was first quantitatively described by G.I. Taylor [1] for laminar flows in a cylindrical tube. These predictions were particularly applicable to times long compared to the one over which a particle diffuses across the width of the tube, here called the Taylor time. From this foundational work, and in a strict analogy to simple Fickian diffusion, a dispersion coefficient could be identified as half the variance of the solute displacement divided by the time; the latter being quadratic in the typical flow speed. Taylor's description was formalised in this laminar tube-flow context by Aris [2], generalised by Brenner and others [3–6], and eventually used to measure diffusion coefficients [7] and influences lab-on-chip design [8].

Such a mature theoretical description of the dispersion complemented with experiments is not available for times short compared to the Taylor time. Nevertheless, several theoretical works [9–13], and some more recent experiments [14–16] were devoted to this short-time limit. These results demonstrate that the dispersion coefficient quadratically increases with time for single-particle observations. However, it is often the case that an ensemble of particles is released from a particular region and their spatio-temporal evolution should be known in detail. Drug delivery from a suddenly rup-

tured nanoparticle [17, 18] provides just one microscopic example. More generally, the efficacy of nanoconfined chemical reactions [19, 20] should critically depend on the time-dependent spatial distribution of reactants. Besides, Taylor dispersion also plays an important role in pulmonary air exchanges [21, 22], the mixing of cerebrospinal fluids [23], DNA molecular mobility [24] and other contexts at the micro- and nano-scales [25–28].

Among the experiments capable of quantitatively accessing short- and long-time dispersion at the nanoscale is total internal reflection fluorescence microscopy (TIRFM). Initially developed for near-surface cell biology [29, 30], TIRFM illuminates a sample with an evanescent wave decaying exponentially from the surface as shown schematically in Fig. 1(a). TIRFM was particularly used to study near-surface colloid/surface interactions in equilibrium [31], following which nanovelocimetry was implemented [32–36], allowing for the quantitative characterization of slip boundary conditions at the nanoscale [32, 37–39], and to study hindered diffusion near a solid/liquid interface [40].

Here we use TIRFM to examine the dispersion of nanoparticle ensembles for a broad range of timescales in a linear shear flow, as shown schematically in Figs. 1(a) and (b). We first demonstrate the quadratic shear-rate dependence of the dispersion coefficient for a linear flow profile. We then study the time dependence, where for short-times the dispersion coefficient increases with time before reaching a long-time plateau predicted using the Taylor method. We find that the transient regime is strongly affected by the grouping of particles: *i*) in

the most general case a mixed-power time dependence is observed for the dispersion coefficient; *ii*) a corresponding linear time dependence can be observed for all-channel, simple-shear protocols; and *iii*) the pure, quadratic time dependence of the dispersion coefficient can be approached by selecting particles in the finest range of altitudes available to the experiment. Analytical modelling allows us to capture the asymptotic behaviours —including an early-time linear-to-quadratic crossover— while Langevin simulations are used to quantitatively recover the full experimental dynamics.

In our experiments —the details of which are found in the Materials and Methods, with the Supporting Information (SI) containing all notations— fluorescent nanoparticles with radius $a = 55$ or 100 nm were advected along the x-direction (*cf.* Fig. 1(b) and SI Video 1) of a pressure-driven flow. Pressure drops $5 \leq \Delta P \leq 400$ mbar were applied across rectangular microchannels with height, $h = 18$ μm, width $w = 180$ μm, and length, $\ell = 8.8$ cm. The fluid viscosities were $1 \leq \eta \leq 7.6$ mPa s, varied by controlling the concentration of glycerol/water mixtures. Given the exponentially decaying evanescent field, we call the apparent altitude $z = \Pi \ln(I_0/I)$ where Π is the exponential decay length, I is the measured particle intensity, as shown in Fig. 1(b), and I_0 is the fluorescence intensity at the wall. Optical aberrations lead to small deviations from an exact exponential decay for the fluorescence intensity, and such details are discussed in the SI. Comparing subsequent images, sample trajectories as in Fig. 1(b) and SI Video 2 were constructed using home-built Matlab routines.

The experimental setup allows the observation of particles in a range of altitudes $a \lesssim z \lesssim 1$ μm from the solid/liquid interface, the solid being a glass coverslip. Here $z = 0$ is set at the solid/liquid boundary and the camera sensitivity determines the upper z-limit. In practice, we do not observe particles for $z \lesssim 200$ nm as a result of electrostatic and steric interactions [31, 41, 42] (see SI for details). The near-surface flow has the advantage of simultaneously exhibiting the lowest velocities $(0 - 600$ μm s$^{-1})$ and largest shear rates $(100 - 600$ s$^{-1})$ as compared to the rest of the channel, offering pertinent conditions for studying the advection-diffusion coupling.

In order to obtain mean velocity profiles along the flow direction over a given lag time, τ, displacements, $\Delta x(z, \tau) = x(z, t + \tau) - x(z, t)$, were measured for each pair of frames for which an identical particle was detected, and taking t as the initial observation time (see Fig. 1(b)). Since the particle intensity encodes the altitude, we first sort the particles into a series of intensity bins, each bin corresponding to a range of approximately 15 nm. Then, the lag-time-independent (verified) streamwise mean velocity $v_x(\bar{z}) = \langle \Delta x(\bar{z}, \tau) \rangle / \tau$ is determined. Here, $\langle \cdot \rangle$ denotes ensemble averaging over *ca.* 10^5 particle observations for each experimental condition accessed for all t. The notation $\bar{\cdot}$ denotes averaging over
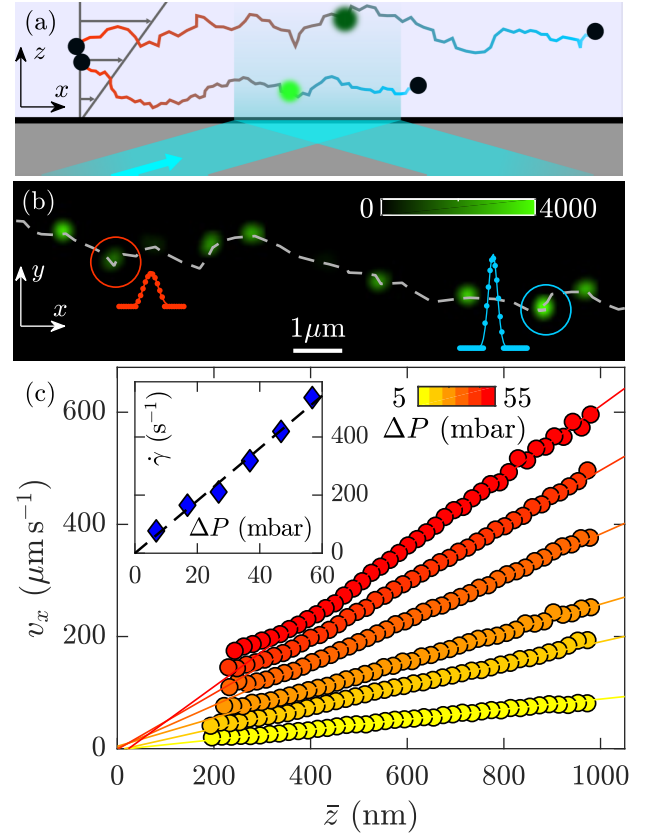

Figure 1: (a) Schematic of two Brownian colloids transported by a near surface shear flow in a microchannel illuminated by an evanescent wave. (b) Superposition of TIRFM images with lag time $\tau = 12.5$ ms, showing successive positions of a fluorescent 55 nm-radius nanoparticle. Two intensity profiles are shown (arbitrary units) with the red and blue dots fitted by Gaussian profiles. The dashed grey line is a guide to the eye. (c) Velocity profiles $v_x = \langle \Delta x \rangle / \tau$ for 55 nm-radius particles as observed in SI Videos 1 and 2 with a lag time $\tau = 2.5$ ms at several pressure drops. The plain lines indicate linear regressions, providing the shear rate value $\dot{\gamma}$. Inset: Shear rate as a function of pressure drop across the microfluidic channel. The dashed black line is a linear regression.

all frames during the lag time.

Figure 1(c) shows the streamwise velocity profiles for 55 nm-radius particles in water and several pressure drops. The solid lines show that the profiles are well approximated by linear functions (see SI and [35, 43] for a discussion of the small non-linearities). The spread of v_x-intercept values arises from the spread of values for I_0 at each pressure, $z = 0$ being taken as the mean of $\Pi \log I_0$ over the different ΔP; $z = 0$ is thus resolved to within 20 nm of the solid/liquid interface assuming no slip [35] as justified in the SI. The low Reynolds numbers (Re $= \rho h U / \eta \approx 10^{-2}$ with ρ the fluid density and U the average velocity in the whole channel) indicate a viscosity-dominated flow for which $v_x(\bar{z}) = \Delta P (\bar{z}^2 - h\bar{z}) / 2\eta L$, *i.e.* a Poiseuille flow. In the region $z \lesssim 1$ μm, and
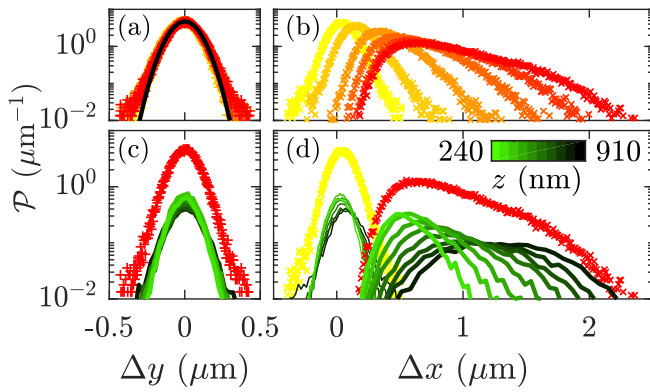
Figure 2: Probability density functions (PDFs) for all transverse (a) and streamwise (b) displacements measured for several pressure drops; the colour code corresponds to the one in Fig. 1(c). The black line in (a) indicates a Gaussian model $\mathcal{P}(\Delta y) = \exp\left(-\Delta y^2/2\sigma_{\Delta y}^2\right)/\sqrt{2\pi\sigma_{\Delta y}^2}$. In (c) the Δy-PDF for the largest pressure drop is decomposed into PDFs for several z. Each green-black PDF corresponds to a z-range of *ca.* 30 nm (some curves omitted for clarity), and the mean value of z is indicated by the colour scale of (d). The decomposed Δx-PDFs for the smallest pressure drop (thinnest green-black lines) and the largest pressure drop (thickest green-black lines) are shown in (d). All the displacements are measured for a time lag $\tau = 2.5$ ms and concern 100 nm-radius particles in water.

given the channel height $h = 18$ μm, the deviation of the Poiseuille profile from linearity is expected to be less than 5 %. Therefore, at first order in $\bar{z}/h$, we have $v_x(\bar{z}) \simeq \dot{\gamma}\bar{z}$, with the shear rate $\dot{\gamma} = \partial_{\bar{z}} v_x|_0 = h|\Delta P|/2\eta L$ and $\partial_{\bar{z}}$ denoting partial differentiation with respect to $\bar{z}$. The inset in Fig. 1(c) shows the shear rate values extracted from the velocity profiles for several pressure drops. As highlighted by the dashed black line, the shear rate increases linearly with the pressure drop. The slope, given by $h/2\eta L$, provides a water viscosity $\eta = 0.9 \pm 0.1$ mPa s at 24 °C in agreement with the expected value [44]. In the SI, we show that $\partial_{|\Delta P|}\dot{\gamma}$ is in quantitative agreement with bulk rheological measurements of the viscosity for all of the liquids investigated here.

Having discussed the mean velocity of the particles, we turn our attention to the displacement distributions. Figures 2(a) and (b) show the probability density functions (PDFs, here called $\mathcal{P}$) of the transverse (Δy) and streamwise (Δx) displacements for 100 nm-radius particles in water over a duration $\tau = 2.5$ ms and several pressure drops. For Fig. 2 and in the following, we systematically take $z = z(t)$, the altitude at the initial observation time. This $z(t)$ should be distinguished from the average $\bar{z}$ over the lag time τ. In Fig. 2(a) it is shown that the transverse displacement PDFs do not depend on the pressure drop and are well described by a Gaussian over two decades. The global standard deviation provides an approximation for the unidimensional Brownian

diffusion coefficient $\sigma_{\Delta y}^2/2\tau \approx 2.0 \pm 0.3$ μm^2 s^{-1}. Despite the lubrication effect discussed below, this estimate is close to the value predicted by the Stokes-Einstein relation $D_0 = k_B T/6\pi\eta a \approx 2.2 \pm 0.2$ μm^2 s^{-1} [45] for particles with $a = 100$ nm advected in water, where k_B is Boltzmann's constant and T is the temperature and η was taken from bulk rheology. Contrasting with the transverse displacement PDFs, those for the streamwise direction in Fig. 2(b) are not Gaussian, become broadened with the pressure drop, and exhibit asymmetry as seen in Ref. [33].

The TIRFM setup provides the particle distance from the glass/liquid interface through the detected intensity, allowing to distinguish the contributions of particles at different altitudes to the global PDFs. In the transverse direction, the local PDFs are shown for the largest pressure drop in Fig. 2(c) and they are all Gaussian regardless of z. In Fig. 2(d) are shown similar decompositions for the smallest and largest pressure drops for streamwise displacements. These decompositions demonstrate that the asymmetry of the global distributions is mainly due to the superposition of different mean displacements at different altitudes. For the smallest pressure drop (yellow) the local PFDs are only slightly shifted with increasing z due to the relatively low mean velocities, *cf.* Fig. 1(c). For the largest pressure drop (red), the mean values are shifted more strongly with increasing z as a result of the higher shear rate. More importantly, the local PDFs thus provide access to the transverse diffusion along y and streamwise dispersion along x for different altitudes.

A detailed study of the local Taylor dispersion as function of time and the various physical parameters at stake is now described. In Figs. 3(a) and (b) are shown the local transverse diffusion coefficient, $D_y(z,\tau) = \sigma_{\Delta y(z)}^2/2\tau$, and the streamwise dispersion coefficient, $\mathcal{D}_x(z,\tau) = \sigma_{\Delta x(z)}^2/2\tau$. The latter comprises pure diffusive and advection effects, and is remarkably larger (up to an order of magnitude) than the former. These data were obtained from altitude decompositions as in Fig. 2 for several τ (red to blue). Figures 3(a) and (b) show that there is a general increase with z of D_y and $\mathcal{D}_x$ until reaching a plateau at large z; in the SI, we show that these plateau values are in quantitative agreement with the Stokes-Einstein relation for all liquids investigated after comparing to independently measured bulk viscosities. The variation with z in both directions is due to hydrodynamic interactions between particles and the solid/liquid interface, leading to a hindered diffusion as discussed in detail elsewhere [40, 46–48]. The z-dependence of D_y is in agreement with the prediction resulting from the effective viscosity near a flat, rigid wall [46] (see the plain black line in Fig. 3(a)). As expected, the transverse diffusion is not dependent on the lag time τ; in contrast, the dispersion coefficients increase significantly with τ as
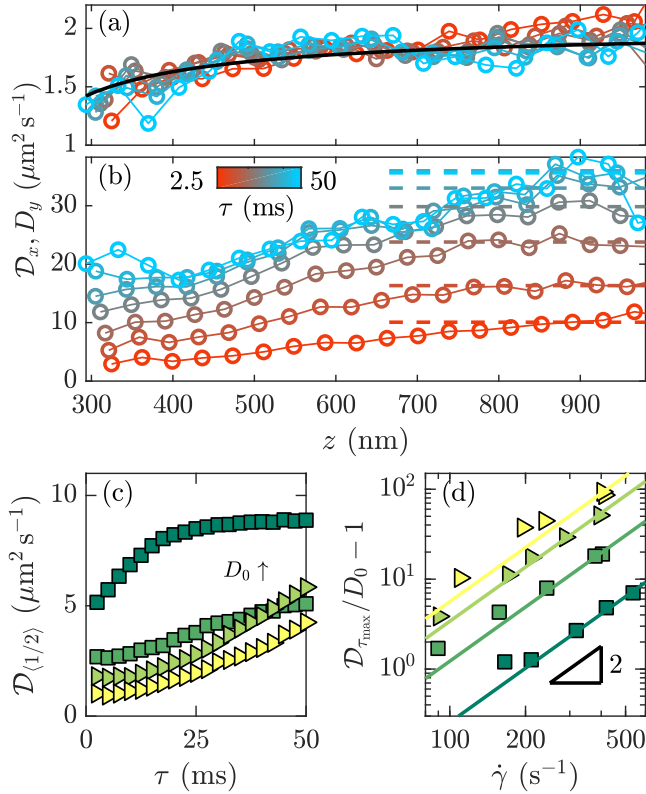
Figure 3: (a) Transverse diffusion coefficients, D_y, and (b) streamwise dispersion coefficient, $\mathcal{D}_x$, as a function the apparent altitude and lag time, τ, for 100 nm-radius particles with a pressure drop of 50 mbar across the microfluidic device. In (a), the plain black line corresponds to the the theoretical prediction $D_y = D_0 \left(1 - (9/16)\,Z^{-1} + (3/8)\,Z^{-3} - (45/256)\,Z^{-4} - (1/16)\,Z^{-5}\right)$ with $Z = z/a$ [46]. In (b) the dashed lines indicate the streamwise dispersion coefficient, $\mathcal{D}_{\langle 1/2 \rangle}$ shown in (c) as a function of lag time. From yellow to dark green, the bulk diffusion coefficient increases. In particular —from bottom to top— the shear rates, particle radii and viscosities are $\{\dot{\gamma}, a, \eta\} = \{110, 100, 7.6\}, \{91, 100, 2.1\}, \{90, 100, 1\}, \{165, 55, 1\}$ in units $\{\mathrm{s}^{-1}, \mathrm{nm}, \mathrm{mPa\,s}\}$; giving $D_0 = \{0.28, 0.89, 2.1, 3.9\}\,\mu\mathrm{m}^2\,\mathrm{s}^{-1}$ determined from the Stokes-Einstein relation. (d) Reduced late-time dispersion coefficient versus the squared shear rate; the solid lines have log-log slope 2.

shown in Fig. 3(b).

In Fig. 3(c) we show the lag-time dependence of the streamwise dispersion coefficient. To do so, we define $\mathcal{D}_{\langle 1/2 \rangle}(\tau)$ as the averaged $\mathcal{D}_x(z(t), \tau)$ for all $z(t) > H/2$, where the length scale, H, is the size of the observation zone. That is, particles beginning their trajectory in the top half of the observation zone, thus limiting the aforementioned lubrication effects. In this figure, the bulk diffusion coefficient D_0 was varied by changing the particle size and the liquid viscosity. For the lowest values of D_0, $\mathcal{D}_{\langle 1/2 \rangle}$ continuously increases with time and the temporal slope increases; by contrast, $\mathcal{D}_{\langle 1/2 \rangle}$ saturates to a plateau for the largest D_0. As explained

by Taylor [1], the time needed to reach the dispersion plateau corresponds roughly to the time needed to diffuse across the channel height. Here the Taylor time is taken as $\tau_z = H^2/D_0$. In a rectangular channel, the exact calculation (see SI) gives a characteristic diffusion time τ_z/π^2. For the 55 nm-radius particles in water, assuming a length scale $H \approx 700$ nm, $\tau_z/\pi^2 \approx 13$ ms, in reasonable agreement with the corresponding data of Fig. 3(c), with $D_0 = 3.9 \pm 0.4$ $\mu\mathrm{m}^2$ s^{-1}. For smaller values of D_0, the dispersion remains mainly in the short-time, increasing-slope regime. Nevertheless, taking the longest-time data available (the data of Fig. 3(c) at $\tau = 50$ ms, denoted $\mathcal{D}_{\tau_{\max}}$) for each D_0 value, we next examine the shear-rate dependence of the dispersion.

In Fig. 3(d) is shown the dependence of the reduced late-time dispersion coefficient, $\mathcal{D}_{\tau_{\max}}/D_0 - 1$, for four D_0 as a function of the shear rate. The solid lines (with slope 2 in log-log representation) show that the reduced $\mathcal{D}_{\tau_{\max}}$ increases quadratically with the shear rate $\dot{\gamma}$ for all D_0 studied. To understand this result, we applied the classical Taylor analysis (i.e. long-time limit, see SI) to a linear shear flow in a rectangular channel, giving

$$\mathcal{D}_x = D_0 \left(1 + \frac{1}{120}\frac{\dot{\gamma}^2 H^4}{D_0^2}\right) \quad \tau \gg \tau_z, \qquad (1)$$

for the infinite-time dispersion coefficient. Identifying $\dot{\gamma}H/2$ as the mean flow velocity in the observation zone with $0 \leq z \leq H$, Eq. 1 is equivalent to the usual result of Taylor, i.e. $\mathcal{D}_x = D_0(1 + \alpha \mathrm{Pe}^2)$ [1]. In this latter expression, the Péclet number is $\mathrm{Pe} = U(H/2)/D_0$, α is a geometry-dependent prefactor and $H/2$ replaces the tube radius of a cylindrical geometry. Equation 1 highlights the key role of velocity gradients in enhanced dispersion, and justifies the linearity of the data in Fig. 3(d) for the 55 nm-radius particles in water. Applying Eq. 1 to this latter data, we extract a length scale $H \approx 500$ nm, consistent with the range of z observed in Fig. 1(c). Because the larger-D_0 data does not reach the infinite-time plateau, the prefactor for the linear regressions does not reveal the corresponding size of the flow region H. However, as we show in the following, the quadratic shear rate dependence is preserved for all time regimes, explaining the scaling of the data in Fig. 3(d).

We now examine the detailed time dependence of dispersion coefficient for all of the experimentally accessed times. Partly inspired by the shear-rate dependence of Fig. 3(d), we show in Fig. 4(a) the reduced $\mathcal{D}_{\langle 1/2 \rangle}$ normalised by $(\tau_z \dot{\gamma})^2$ as a function of the dimensionless lag time, τ/τ_z. Remarkably, the data in Fig. 3(c), along with that for experiments implementing four other shear rates per D_0, collapse onto a single master curve. Such a collapse suggests the existence of a universal function describing the reduced dispersion coefficient. While in Figs. 3(c),(d) and Fig. 4(a), we consider particles beginning their trajectories in the top half of the channel, this fraction can be generalised, with n representing the frac-
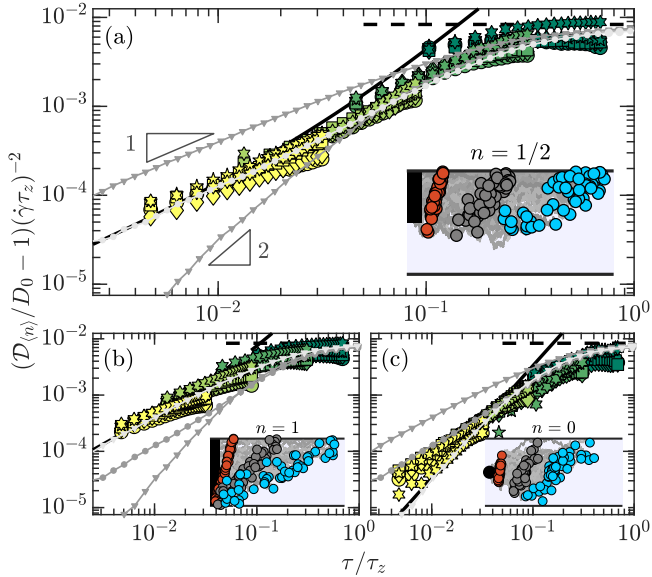
Figure 4: Reduced dispersion coefficient as a function of dimensionless time for all shear rates and D_0 studied for fractions (a) $n = 1/2$, (b) $n = 1$, and (c) $n \to 0$ of the observation zone. The bulk diffusion coefficients, D_0, for the data from dark green to yellow points are identical to those in Figs. 3(c) and (d). The black dashed and solid lines respectively correspond to the asymptotic behaviours for the long- and short-time regimes predicted by Eqs. 1 and 3. The gray lines decorated with circles and triangles correspond to the results from Langevin simulations for the $n = 1/2$, $n = 1$ and $n = 0$ conditions. For each panel, the corresponding simulation results are highlighted in lighter gray. The insets schematically show three instants of particle trajectories advected from the associated observation zone in a linear shear flow and with diffusion in z. The slope triangles in (a) denote power-law exponents 1 and 2.

tion of the observation zone from which particles leave, with $0 \le n \le 1$. The reduced dispersion is thus expected to follow a relation of the form

$$\left(\frac{\mathcal{D}_{\langle n \rangle}}{D_0} - 1 \right) (\dot{\gamma} \tau_z)^{-2} = \mathcal{F}_{\langle n \rangle} \left(\frac{\tau}{\tau_z} \right) . \quad (2)$$

Examining Fig. 4(a), we note that the reduced $\mathcal{D}_{\langle 1/2 \rangle}$ increases with time and then reaches a plateau. According to Eq. 1, in the $\tau/\tau_z \to \infty$ limit, $\mathcal{F}_{\langle n \rangle}$ is expected to reach $1/120$. This value is shown with the horizontal black dashed line and is in quantitative agreement with the data which crosses over when $\tau/\tau_z \approx 1$.

Concerning the data at the shortest dimensionless lag times in Fig. 4(a), we find that they do not follow the typically predicted [9–13] and measured [14–16] early-time τ^2 dependence. A key foundation of this τ^2 dependence is the assumption that each particle begins its trajectory at the same initial altitude. In general, however, particles may leave from a non-peaked distribution of initial altitudes. This distribution is particularly relevant for Fig. 4(a), since the plotted quantity is related to an aver-

age of all the particles in the top half of the observation zone (indicated by the dashed lines in Fig. 3(b)).

To investigate the effect of such a distribution of initial particle altitudes, we proceed by assuming that particles are 'released' at time t and position z_0 from a general distribution $\mathcal{P}_0(z_0)$ in an infinitely extended shear flow. This description should thus be valid for early times only. Given such a distribution of initial altitudes, the linear shear flow, and diffusion along the z-direction, we analytically demonstrate that Eq. 2 is the appropriate form for the lag-time-dependent, reduced short-time dispersion coefficient (see SI). In the simple case for which particles are uniformly released over a fraction n of the channel height, the function $\mathcal{F}_{\langle n \rangle}$ becomes:

$$\mathcal{F}_{\langle n \rangle} \left(\frac{\tau}{\tau_z} \right) = \frac{n^2}{24} \left(\frac{\tau}{\tau_z} \right) + \frac{1}{3} \left(\frac{\tau}{\tau_z} \right)^2 , \quad \tau \ll \tau_z . \quad (3)$$

The more general case of a non-uniform initial distribution of altitudes is also captured by our model. In that case, the prefactor of the linear term in τ/τ_z on the right-hand-side of Eq. 3 is replaced with the initial variance of the distribution normalized by the mean-square displacement in the vertical direction over the Taylor time:

$$\frac{n^2}{24} \to \frac{\langle z_0^2 \rangle - \langle z_0 \rangle^2}{2 D_0 \tau_z} . \quad (4)$$

We now examine the limits of Eqs. 3 and 4. A null variance of the initial distribution arises if all particles start at the same altitude (here called the "dot" condition). For this dot condition, the classical τ^2 dependence for the reduced short-time dispersion coefficient is recovered, reflecting a steadily increasing diversity of newly sampled velocities (see SI Videos 3 and 4). The dot condition corresponds to single-particle tracking in a linear shear flow, as considered before [9–16]. For non-vanishing initial variance, the reduced dispersion coefficient has a linear temporal evolution at times shorter than the crossover time $\tau_C = 3(\langle z_0^2 \rangle - \langle z_0 \rangle^2)/2 D_0$ obtained by setting the linear and quadratic terms of Eq. 3 to be equal. This linear behaviour for extended distributions results from particles at different altitudes transported different distances by the linear shear flow (SI Videos 3 and 4). When the initial variance is small with respect to H^2, a crossover into the quadratic lag-time dependence occurs, before the Taylor plateau for the observation zone is reached.

In Fig. 4(a), we consider particles leaving from the upper half of the observation zone, as schematically shown in the inset. The corresponding analytical prediction of Eqs. 2 and 3 with $n = 1/2$ is also shown in Fig. 4(a) as a black solid line. At early times, the prediction of the analytical model is in good agreement with the experimental data choosing the observation zone to be that which comprises 90 % of our particle observations.

To understand the complete time dependence including the long-time Taylor saturation, we performed numerical integrations of the overdamped Langevin equations used in [35, 49]. Here we assumed an effective channel with reflecting boundary conditions at both walls and a linear shear flow between them. For the case $n = 1/2$ (called the "half-line" condition), the reduced dispersion coefficients from these simulations are shown in Fig. 4(a) in light gray. The predictions from the Langevin equations show a complete, quantitative agreement with the experimental data with no fitting parameter. For comparison, we have also simulated cases with $n = 0$ (dot) and $n = 1$ (called the "line" condition), which at early times are well outside the experimental data limits. Furthermore, we observe that the half-line simulation is parallel to the line-condition simulation at the earliest times, and joins the simulation results for the dot and line conditions at later times. These observations are consistent with the main features of the analytical model described above (i.e. the linear-to-quadratic crossover). While the analytical model and the simulation ignore electrostatic and hydrodynamic interactions with the wall, in the SI we show that these phenomena respectively reduce the size of the effective channel but do not affect the main features of time-dependent advection-diffusion coupling discussed here.

In order to test our analytical model, we again leverage the depth resolution of the TIRFM method to select different initial distributions. First, we choose the line condition illustrated in the inset of Fig. 4(b). We thus study the dispersion coefficients for all observed particles, meaning that we consider the global distributions of Fig. 2(b). The reduced dispersions measured for this condition are shown in Fig. 4(b). The results are once again in quantitative agreement with the early-time, analytical prediction and the full-time Langevin simulations. Similarly, we consider particles leaving from a narrow altitude range, approaching the dot condition (inset of Fig. 4(c)). In Fig. 4(c) is shown the corresponding temporal evolution of the reduced dispersion coefficient for $z_0 = 600 \pm 15$ nm. While the data does not reach exactly (especially at early times) the theoretical prediction for the dot condition due to the polydispersity of the particles (and thus non-unique altitudes for a given intensity [43]), it is systematically below the one for the half-line condition and approaches the τ^2 asymptotic behaviour predicted by Eq. 3 for $n = 0$. The experimental data also agrees well with the corresponding Langevin simulation results. The data analysis and numerical simulations carried out for three different initial particle distributions using the same measurement data clearly demonstrate the crucial role of such a distribution for the short-time dispersion. Furthermore, these results validate our novel analytical model, that can be used to quantitatively rationalise general short-time dispersion observations.

To conclude, we report on an experimental, theoreti-cal, and numerical study of advection-enhanced dispersion from short to long times compared to the classical Taylor time. We provide a quantative description of the short- and long-time dispersion behaviours. First, we show that the two regimes share the same shear-rate dependence, the shear rate being particularly large for near-surface transport where the advection-diffusion coupling should be the largest. Furthermore, we reveal and characterize how the initial particle distribution affects the short-time dispersion. Specifically, we observe a short-time, mixed-power-law behaviour for the general case, before a crossover to the well-known long-time saturation regime for linear shear flows. In the extremal cases of i) full-channel observations, a linear approach of the dispersion coefficient to the long-time value is observed, while ii) for fine depth resolutions a quadratic tendency is approached. Altogether, the experimental data are in quantitative agreement with the analytical predictions and results from Langevin numerical simulations. In the rich context of particle transport, such concepts should prove pertinent in quantitative prediction and observation of time-dependent, near-surface nanoparticle and solute dispersion, with applications related to microscopic biology and nanoscale technologies.

METHODS

All the experiments performed here employed pressure-driven flows (Fluigent MFCS-4C pressure controller) in microchannels with a rectangular section (height $h = 18$ μm, width $w = 180$ μm, length $\ell = 8.8$ cm). Microfluidic chips were fabricated by soft lithography of poly(dimethyl siloxane) (Dow Chemical, Sylgard 184) on a plasma-cleaned glass coverslip with 145 μm thickness constituting the bottom surface. The liquids used were ultra-pure water (18.2 MΩ cm, MilliQ) and water-glycerol mixtures that gave Newtonian fluids with Newtonian viscosities of $\eta = 1, 2.1$ and 7.6 mPa s, measured with a Couette-cell rheometer (Anton Paar MCR 302) up to $\dot{\gamma} = 1000$ s^{-1}. The fluorescent nanoparticles used were 55 nm-radius (Invitrogen F8803, Thermofisher) and 100 nm-radius (Invitrogen F8888 Thermofisher) latex microspheres used without further modification besides dilution by a factor of 10^3 using utra-pure water.

TIRFM measurements were realised by illuminating the near-surface shear flow with a laser source (Coherent Sapphire, wavelength $\lambda = 488$ nm, power 150 mW) focused off the central axis of, and on the back focal plane of a $100\times$ microscope objective with a large numerical aperture (NA = 1.46, Leica HCX PL APO). Large NA is required to reach incident angles θ larger than the critical angle, $\theta_c = \arcsin(n_l/n_g)$, enabling total reflection at the glass/liquid interface. Here, $n_g = 1.518$ is the refractive index of the glass coverslip, n_f is the refractive index of

the liquid and θ the angle of incidence of the laser; the refractive indices of the three liquids were measured using a refractometer (Atago PAL-RI).

The complete setup and alignment procedure are described in [50]. In the TIRFM configuration, the evanescent wave has an intensity decaying exponentially as $I(z) = I_0 \exp(-z/\Pi)$ with the penetration depth $\Pi = (\lambda/4\pi)\left(n_g^2 \sin^2\theta - n_f^2\right)^{-1/2}$. Typical values of the penetration depth were thus $\Pi \approx 100$ nm, allowing for an observation of particles roughly within the first micrometer from the glass/liquid interface whereas the channel height is $h = 18\ \mu$m. The images of 528×512 pixels (px), with 22.9 px/μm, are recorded in 16-bit format (Andor Neo sCMOS) with a frame rate of 400 Hz for a duration of 5 s. For each set of parameters (particle radius, viscosity and pressure drop), five videos of 2000 frames were recorded. Fig. 1(b) shows a superposition of 18 frames showing a single 55 nm-radius particle's near-surface trajectory in a water flow with an imposed pressure drop of 30 mbar across the microfluidic device. After a centroid detection, the intensity profile was fitted by a radially-symmetric Gaussian model for each frame. Thus the x and y coordinates give the particle position in the plane parallel to the glass/water interface whereas the particle height, z, is encoded in the intensity thanks to the exponential decay of the evanescent wave. The apparent altitude is $z = \Pi \log(I_0/I)$ [35, 43]. A discussion linked to the limitations of using this apparent altitude appears in the SI.

[1] G. I. Taylor, Proceedings of the Royal Society of London. Series A. Mathematical and Physical Sciences **219**, 186 (1953).

[2] R. Aris, Proceedings of the Royal Society of London. Series A. Mathematical and Physical Sciences **235**, 67 (1956).

[3] H. Brenner and D. Edwards, *Macrotransport Processes, edited by Butterworth* (Heinemann, 1993).

[4] H. A. Stone and H. Brenner, Industrial & Engineering Chemistry Research **38**, 851 (1999).

[5] R. R. Biswas and P. N. Sen, Physical Review Letters **98**, 164501 (2007).

[6] I. Griffiths and H. A. Stone, EPL (Europhysics Letters) **97**, 58005 (2012).

[7] M. S. Bello, R. Rezzonico, and P. G. Righetti, Science **266**, 773 (1994).

[8] C. L. Hansen, M. O. Sommer, and S. R. Quake, Proceedings of the National Academy of Sciences **101**, 14431 (2004).

[9] T. Van de Ven, Journal of Colloid and Interface Science **62**, 352 (1977).

[10] G. Batchelor, Journal of Fluid Mechanics **95**, 369 (1979).

[11] R. Foister and T. Van De Ven, Journal of Fluid Mechanics **96**, 105 (1980).

[12] C. Van den Broeck, J. Sancho, and M. San Miguel, Physica A: Statistical Mechanics and its Applications **116**, 448 (1982).

[13] K. Miyazaki and D. Bedeaux, Physica A: Statistical Mechanics and its Applications **217**, 53 (1995).

[14] H. Orihara and Y. Takikawa, Physical Review E **84**, 061120 (2011).

[15] E. O. Fridjonsson, J. D. Seymour, and S. L. Codd, Physical Review E **90**, 010301 (2014).

[16] Y. Takikawa, T. Nunokawa, Y. Sasaki, M. Iwata, and H. Orihara, Physical Review E **100**, 022102 (2019).

[17] F. Gentile, M. Ferrari, and P. Decuzzi, Annals of Biomedical Engineering **36**, 254 (2008).

[18] J. Tan, A. Thomas, and Y. Liu, Soft Matter **8**, 1934 (2012).

[19] T. K. Nielsen, U. Bösenberg, R. Gosalawit, M. Dornheim, Y. Cerenius, F. Besenbacher, and T. R. Jensen, ACS Nano **4**, 3903 (2010).

[20] A. B. Grommet, M. Feller, and R. Klajn, Nature Nanotechnology **15**, 256 (2020).

[21] J. J. Fredberg, Journal of Applied Physiology **49**, 232 (1980).

[22] J. Grotberg, Annual Review of Fluid Mechanics **26**, 529 (1994).

[23] L. Salerno, G. Cardillo, and C. Camporeale, Physical Review Fluids **5** (2020).

[24] D. Stein, F. H. van der Heyden, W. J. Koopmans, and C. Dekker, Proceedings of the National Academy of Sciences **103**, 15853 (2006).

[25] R. Bearon and A. Hazel, Journal of Fluid Mechanics **771** (2015).

[26] S. Marbach, K. Alim, N. Andrew, A. Pringle, and M. P. Brenner, Physical Review Letters **117**, 178103 (2016).

[27] S. Marbach and K. Alim, Physical Review Fluids **4**, 114202 (2019).

[28] A. Dehkharghani, N. Waisbord, J. Dunkel, and J. S. Guasto, Proceedings of the National Academy of Sciences **116**, 11119 (2019).

[29] D. Axelrod, The Journal of cell biology **89**, 141 (1981).

[30] K. N. Fish, Current Protocols in Cytometry **50**, 12 (2009).

[31] D. C. Prieve, Advances in Colloid and Interface Science **82**, 93 (1999).

[32] R. Pit, H. Hervet, and L. Léger, Physical Review Letters **85**, 980 (2000).

[33] S. Jin, P. Huang, J. Park, J. Yoo, and K. Breuer, Experiments in Fluids **37**, 825 (2004).

[34] M. Yoda and Y. Kazoe, Physics of Fluids **23**, 111301 (2011).

[35] Z. Li, L. D'eramo, C. Lee, F. Monti, M. Yonger, P. Tabeling, B. Chollet, B. Bresson, and Y. Tran, Journal of Fluid Mechanics **766**, 147 (2015).

[36] M. Yoda, Annual Review of Fluid Mechanics **52**, 369 (2020).

[37] P. Huang, J. S. Guasto, and K. S. Breuer, Journal of Fluid Mechanics **566**, 447 (2006).

[38] D. Lasne, A. Maali, Y. Amarouchene, L. Cognet, B. Lounis, and H. Kellay, Physical Review Letters **100**, 214502 (2008).

[39] C. Bouzigues, P. Tabeling, and L. Bocquet, Physical Review Letters **101**, 114503 (2008).

[40] P. Huang and K. S. Breuer, Physical Review E **76**, 046307 (2007).

[41] B. Derjaguin, Transactions of the Faraday Society **35**, 203 (1940).

[42] E. J. W. Verwey, The Journal of Physical Chemistry **51**, 631 (1947).

[43] X. Zheng, F. Shi, and Z. Silber-Li, Microfluidics and Nanofluidics **22**, 127 (2018).

[44] L. Korson, W. Drost-Hansen, and F. J. Millero, The Journal of Physical Chemistry **73**, 34 (1969).

[45] A. Einstein, Annalen der Physik **322**, 549 (1905).

[46] H. Brenner, Chemical engineering science **16**, 242 (1961).

[47] L. P. Faucheux and A. J. Libchaber, Physical Review E **49**, 5158 (1994).

[48] A. Saugey, L. Joly, C. Ybert, J.-L. Barrat, and L. Bocquet, Journal of Physics: Condensed Matter **17**, S4075 (2005).

[49] D. L. Ermak and J. A. McCammon, The Journal of Chemical Physics **69**, 1352 (1978).

[50] M. T. Hoffman, J. Sheung, and P. R. Selvin, in *Single Molecule Enzymology* (Springer, 2011), pp. 33–56.